Subband structure and mobility of two-dimensional holes in strained Si/SiGe MOSFET's

R. Oberhuber, G. Zandler, and P. Vogl
Physik-Department and Walter Schottky Institut, Technische Universität München, Am Coulombwall, D-85748 Garching, Germany
(Received 12 May 1998)

The hole mobility of p-type strained Si metal-oxide-semiconductor field-effect transistors (MOSFET's) fabricated on a SiGe substrate is investigated theoretically and compared with the mobility of conventional (unstrained) Si p-MOSFET's. Two-dimensional quantization of the holes is taken into account in terms of a self-consistent six-band $\mathbf{k}\cdot\mathbf{p}$ model for the strained band structure and the confined hole subband states in the inversion channel. The hole dynamics along the inversion channel is studied in terms of ensemble Monte Carlo calculations that take into account all relevant scattering mechanisms. For a Ge concentration of 30% in the substrate, we predict a mobility enhancement of a factor of 2.3 compared to the unstrained p-type device. The calculated low-field mobility is in excellent agreement with experimental data for strained $Si/Si_{0.8}Ge_{0.2}$ and for unstrained Si p-MOSFET's. [S0163-1829(98)10635-5]

I. INTRODUCTION

Two-dimensional electron transport in Si n-type metal-oxide-semiconductor field-effect transistors (MOSFET's) has been studied experimentally and theoretically for many years and in great detail.[1–4] Surprisingly, rather few theoretical studies have been published so far that focus on the hole transport in p-type Si inversion channels. In part, this is due to the complex valence-band structure of Si, but it also has purely practical reasons. Standard p-type MOSFET devices have much poorer transport characteristics than n-type devices—mainly[5] due to the heavy effective hole masses—which made them less relevant for accurate device modeling.

Recently, however, the growth of pseudomorphic strained Si and Si_xGe_{1-x} structures has created a new degree of freedom for tailoring transport characteristics of n-type as well as p-type MOSFET devices. While strain and alloying makes a quantitative transport analysis even more complex, it has now become highly relevant to assess the potential of this new degree of freedom for improving p-type Si devices.

In this paper, we present a detailed theoretical analysis of hole mobilities in strained Si/SiGe inversion layers that quantitatively takes into account the electronic states of the quantum-confined holes as well as the Boltzmann carrier dynamics. We employ a self-consistent multiband $\mathbf{k}\cdot\mathbf{p}$ method for the electronic subband structure of the confined holes and take into account inter- and intrasubband phonon, remote-impurity, and interface roughness scattering in terms of an ensemble Monte Carlo procedure. The only major simplification in our calculations is the assumption of a spatially homogeneous inversion channel.

In bulk strained Si and SiGe alloys, the semiclassical transport of n- as well as p-type material has been studied in terms of elaborate full-band Monte Carlo calculations.[6–8] These calculations showed very significant improvements in the electron and hole mobility of biaxially strained Si grown on a SiGe substrate. This is due to the lifting of the band-edge degeneracies that affects the transport masses and reduces intervalley or interband scattering.

For n-type Si inversion layers, it has been shown by detailed theoretical calculations that the effect of the carrier quantization due to the confining electric field, the Si/oxide interface induced scattering, as well as the two-dimensional carrier screening can give mobilities that substantially differ from bulk values.[3] Simpler model calculations show qualitatively similar trends for electrons[4] in strained Si inversion layers and for holes[9] in unstrained Si. However, to the best of our knowledge, no calculations for strained p-type Si/SiGe inversion layers have been published yet.

In Sec. II, we discuss the geometry and material compositions of the p-type MOSFET structures that we consider in this paper. The theoretical methods employed are briefly summarized in Sec. III. The electronic structure calculations are based on a self-consistent multiband $\mathbf{k}\cdot\mathbf{p}$ method (Sec. III) and the carrier dynamics is computed in terms of a momentum-space Monte Carlo method that is discussed in Sec. IV. The scattering mechanisms are summarized in Secs. IV A and IV B, and the equations of motion in Sec. IV C. After briefly discussing the numerical details in Sec. V, we present results (Sec. VI) for the self-consistently determined confined hole subbands in Sec. VI A, hole drift velocity and energy (Sec. VI B), and finally, the hole mobility in unstrained as well as in strained Si/SiGe structures in Secs. VI C and VI D, respectively. A summary in Sec. VII concludes the paper.

II. STRAINED p-TYPE MOSFET STRUCTURES

We consider p-channel MOS structures such as shown schematically in Fig. 1. Beneath the gate oxide, we assume a 15 nm layer of [001] strained Si that is grown pseudomorphically on a fully relaxed SiGe buffer. The stress is provided by the buffer that sets the in-plane lattice constant that is larger than in bulk Si. Both regions are assumed to be homogeneously n doped. We consider a doping concentration of 5×10^{16} cm^{-3}. Such a structure can be fabricated by the ''graded-buffer concept'' (see, e.g., Refs. 8 and 10) or by ''silicon-on-insulator technology.''[11] The subband structure and the channel density is determined by an interplay between strain, confinement, and doping effects that in turn determines the mobility along the channel. We will compute the subband structure beneath the gate by a self-consistent

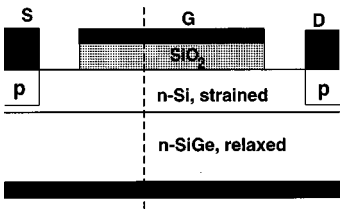

FIG. 1. Schematic geometry of strained Si/SiGe p-MOS transistors. The buffer consists of strain-relaxed SiGe that determines the lateral lattice constant of the Si layer beneath source (S), gate (G), and drain (D) contacts. The quantization of electronic states is calculated along the dashed line.

solution of the one-dimensional Schrödinger and Poisson equation (along the dashed line depicted in Fig. 1) and subsequently evaluate the lateral transport by solving the full Boltzmann transport equation with a Monte Carlo technique. Since we are mainly interested in the low-field mobility, the lateral variation of the sheet carrier density between source and drain is neglected.

III. ELECTRONIC STRUCTURE CALCULATIONS

The theoretical concepts that have been employed for computing the electronic structure in strained p-type Si inversion layers are briefly summarized in this section.

k·p method

We use a many-band $\mathbf{k}\cdot\mathbf{p}$ procedure to solve the one-dimensional Schrödinger and Poisson equation self-consistently along the growth direction that will be denoted by z. Since we focus on p-type channel devices, only the top six valence-band states are treated quantum mechanically, whereas a classical Thomas-Fermi approximation is used for the electrons. Let us consider a strained Si or SiGe bulk semiconductor first. In this case, the Schrödinger equation for the six envelope functions $F_n(z)$, $(n=1,\ldots,6)$ reads in the standard 6×6 $\mathbf{k}\cdot\mathbf{p}$ Kohn-Luttinger and Bir-Pikus basis,[12–14,16]

$$\sum_{n=1}^{6}\left[D_{mn}^{(2)\alpha\beta}k_\alpha k_\beta + D_{mn}^{(0)}\right]F_n = EF_m. \tag{1}$$

The Cartesian indices α,β are being summed over. The term $D_{\mu\nu}^{(0)}$ includes the band-edge deformation potentials. We note that the eigenvalues of this six-band $\mathbf{k}\cdot\mathbf{p}$ matrix for bulk strained Si deviate by less than 10% from full band structure results[15] up to energies of 0.5 eV away from the band edge.

In order to determine the electronic structure of strained Si/SiGe heterostructures, we augment Eq. (1) by the electrostatic potential $V_H(z)$ due to the space charge that is to be calculated self-consistently, and by the piecewise constant band offset contribution $V_{offs}(z)$. In addition, we invoke the standard Kohn-Luttinger approach[16,17] and take into account the loss of translational invariance along the z direction by replacing the wave vector-component k_z by the operator $k_z = -i\partial/\partial z$. It is therefore convenient to separate out all terms proportional to k_z in the Hamiltonian Eq. (1) and to write the resulting expression in a symmetrized form,[18–20]

TABLE I. Electronic structure related material parameters used in this work, and compared to previously determined values. ΔE_v is the band discontinuity of the topmost valence bands of strained Si on fully relaxed Ge, b is the shear deformation potential, and L, M, N are the bulk Luttinger valence-band parameters.

Material	Parameter	Present work	Literature
Si:Ge	ΔE_v (eV)	0.17	0.17, [a] 0.17, [b] 0.22, [c] 0.21 [d]
Si	b (eV)	−2.1	−1.5, [e] −2.1, [f] −2.2, [g] −2.33, [h] −2.12, [i] −2.35, [j] −2.58, [k] −2.27 [l]
	L	−6.64	−6.69, [h] −5.53, [m] −6.64 [n]
	M	−4.60	−4.62, [h] −3.64, [m] −4.60 [n]
	N	−8.68	−8.56, [h] −8.32, [m] −8.68 [n]
Ge	L	−31.34	−21.65, [h] −30.53, [m] −31.34 [n]
	M	−5.90	−5.02, [h] −4.64, [m] −5.90 [n]
	N	−34.14	−23.48, [h] −33.64, [m] −34.14 [n]

[a]Reference 21.
[b]Reference 22.
[c]Reference 23.
[d]Reference 24.
[e]Reference 25.
[f]Reference 26.
[g]Reference 27.
[h]Reference 15.
[i]Reference 28.
[j]Reference 29.
[k]Reference 30.
[l]Reference 31.
[m]Reference 6.
[n]Reference 32.

$$\mathbf{H}(\mathbf{k}) = \sqrt{\mathbf{H}^{(2)}}k_z^2\sqrt{\mathbf{H}^{(2)}} + \frac{1}{2}\left[k_z\mathbf{H}^{(1)}(\mathbf{k}) + \mathbf{H}^{(1)}(\mathbf{k})k_z\right] + \mathbf{H}^{(0)}(\mathbf{k}) + \left[V_{offs}(z) + V_H(z)\right]\mathbf{1},$$
$$\sum_{n=1}^{6} H_{mn}(\mathbf{k})F_n^\nu = E_\nu F_m^\nu, \tag{2}$$

where $\mathbf{k} = (k_x, k_y)$ is the in-plane wave vector and the index ν labels the subbands associated with the top valence bands $m,n=1,\ldots,6$. This Hermitian form of the Hamiltonian is equivalent to current conserving boundary conditions for the envelope functions F_m^ν at each heterostructure interface.[17–20] We note that the terms $\mathbf{H}^{(2)}$, $\mathbf{H}^{(1)}$, and $\mathbf{H}^{(0)}$ are independent of position within a given heterostructure layer. All band parameters for Si and Ge that enter this Hamiltonian are summarized in Table I and these values have been interpolated for $Si_{1-x}Ge_x$ according to Ref. 15. The biaxial strain that characterizes the pseudomorphic growth of Si on (001)-oriented SiGe substrates is determined by the elastic constants c_{11} and c_{12} and the bulk lattice constants. These are given in Table II for the pure materials Si and Ge. In the alloy, the elastic constants are interpolated linearly while the bulk lattice constant is taken from experiment.[33]

We have employed standard current conserving boundary conditions[17] for the $\mathbf{k}\cdot\mathbf{p}$ Hamiltonian matrix at the Si/SiGe interface and assume that the image potential cancels the many-body corrections given by the exchange and correlation terms of $V_H(z)$.[1,3] At the oxide and deep inside the SiGe substrate, we set to zero all envelope functions. While this has been shown to become invalid for ultrathin structures,[34] this approximation is well justified for the size of layers studied here.

TABLE II. Material parameters used in this work. All values are taken from the compilation of Ref. 32.

Quantity	Symbol	Units	Si	Ge
Lattice constant	a_0	Å	5.43	5.65
Density	ρ	g cm^{-3}	2.33	5.32
Elastic constants	c_{11}	10^{11} dyn cm^{-2}	16.577	12.853
	c_{12}	10^{11} dyn cm^{-2}	6.393	4.826
Γ_{7v}-Γ_{8v} spin orbit Splitting	Δ_{so}	meV	44.0	296.0
Dielectric constant	ϵ_{sc}		11.9	16.0
Dielec. constant SiO_2	ϵ_{ox}		3.9	

The electrostatic potential $V_H(z)$ of Eq. (1) is determined by the charge of the holes in the Si inversion layer and the free electrons in the SiGe substrate via the Poisson equation,

$$-\frac{\partial^2 V_H(z)}{\partial z^2}=\frac{e}{\epsilon}[p(z)-n(z)+N_D(z)], \tag{3}$$

with the density of donors N_D and the dielectric constant ϵ. The hole and electron carrier concentration is given by

$$p(z)=\sum_\nu \frac{1}{2\pi^2}\int d\mathbf{k} f(E_F-E_\nu(\mathbf{k}))|\zeta_\nu(\mathbf{k},z,\mathbf{r})|^2,$$

$$n(z)=\frac{1}{4\pi^3}\int d\mathbf{k}dk_z f(E_c(\mathbf{k},k_z)+V_{offs}(z)-V_H(z)-E_F), \tag{4}$$

respectively, where f is the Fermi distribution function, E_F the Fermi energy, k_B the Boltzmann constant, T the lattice temperature, and E_{ck} the parabolic bulk conduction-band energy. The envelope functions ζ_ν corresponding to valence subband ν are given by

$$\zeta_\nu(\mathbf{k},\mathbf{r},z)=\frac{1}{\sqrt{L}}\sum_{n=1}^{6} F_n^\nu(\mathbf{k},z)e^{i\mathbf{k}\cdot\mathbf{r}}, \tag{5}$$

where $\mathbf{r}$ is the lateral real space vector and L is the normalization length. Since we consider an impenetrable oxide layer beneath the gate (zero current approximation), the Fermi energy is constant and is determined by the substrate doping concentration.

IV. MOBILITY CALCULATIONS

First, we present the calculated hole scattering rates that have been obtained in terms of the quantized subband wave functions and energies discussed in the previous section. Subsequently, we discuss a momentum-space ensemble Monte Carlo procedure to compute the hole transport in the quantized two-dimensional (2D) channel that consistently invokes the computed 2D scattering rates. For electrons and a single conduction band, a similar procedure was carried out previously in Ref. 3.

A. Hole-phonon interaction

By using the wave functions from Sec. III, we obtain the following expression for the interaction between 2D holes and bulk phonons within deformation potential theory that includes both intra- and intersubband scattering. The scattering rate between a hole at state μ, $\mathbf{k}$ into subband and wave vector ν, $\mathbf{k}+\mathbf{q}$ and a phonon of type $j\mathbf{q}$ is given by

$$\Gamma_{\mu,\nu}(\mathbf{k},\mathbf{k}+\mathbf{q}|j,\mathbf{q})=\frac{\pi}{\rho\omega_{j,\mathbf{q}}}\Delta_j^2|J_{\mu\nu}(\mathbf{k},\mathbf{q},q_z)|^2 \times\delta(E_\mu(\mathbf{k})-E_\nu(\mathbf{k}\pm\mathbf{q})\pm\hbar\omega_{j,\mathbf{q}}) \times\left(\frac{1}{2}\mp\frac{1}{2}+n_{j,\mathbf{q}}\right). \tag{6}$$

Here, the signs indicate phonon emission and absorption, respectively, ρ is the mass density, $n_{j,\mathbf{q}}$ represents the phonon occupation number, Δ_j is the angular averaged deformation potential coupling constant that we take from unstrained bulk, and $\omega_{j,\mathbf{q}}$ is the phonon frequency. The electronic overlap factor is given by

$$J_{\mu\nu}(\mathbf{k},\mathbf{q},q_z)=\int_0^\infty \zeta^\nu(\mathbf{k}\pm\mathbf{q},z)\exp[-i(\mathbf{q}\cdot\mathbf{r}+q_z z)] \times\zeta^\mu(\mathbf{k},z)dz. \tag{7}$$

This expression generalizes the standard Bloch overlap factor that enters the bulk scattering rates for holes.[35] We have taken into account Eq. (6) for acoustic and optic phonons with intra- as well as intersubband scattering for approximately 40 subbands (see Sec. V). For acoustic phonons, the scattering process has been treated elastically, which is suitable at room temperature.

For comparison, we have also evaluated Eq. (6) with an effective one-hole band model, where all subbands have been assumed to be characterized by the same lateral density-of-states effective mass. Optimal effective mass values that reproduce the fully nonparabolic results will be given in Sec. VI B.

B. Interface roughness and Coulomb scattering

Scattering due to Si-SiO_2 interface roughness scattering has been included according to a model proposed by Goodnick *et al.*[36–38] We have generalized this model for the present case of confined 2D holes by taking into account intra- and intersubband scattering as determined by the overlap factor Eq. (7). The interface scattering model characterizes the interface by two parameters, the rms step height Δ and the autocorrelation function of the step distance Λ. The parameters are listed in Table III; they enter the calculations only for Si since the carriers are confined to a narrow region within the strained layer.

At room temperature and for relevant carrier concentrations in the channel, the mobility is dominated by phonon and interface roughness scattering. We have therefore incorporated impurity scattering only within a simple Brooks-Herring type expression[47] that takes into account screening

TABLE III. Carrier scattering related parameters for Si used in this work, and compared to previously determined values. Ξ_{ac}^{eff} and Δ_{op} are the average valence-band edge acoustic and optic deformation potentials, respectively, $\hbar\omega_{op}$ is the phonon energy, and Λ and Δ characterize the interface roughness.

Phonon scattering	Present work	Literature
Ξ_{ac}^{eff} (eV)	5.0	3.1, [a] 4.0, [b] 5.0, [c] 6.2 [d]
Δ_{op} (10^8 eV cm^{-1})	7.63	7.63, [e] 6.0, [b] 7.29, [f] 9.05, [a] 10.5 [g]
$\hbar\omega_{op}$ (meV)	61.2	61.2, [h] 62.8 [f]
Interface roughness scattering		
Λ (Å)	20.0	220.0, [i] 22.0, [j] 13.0, [k] 15.0 [l]
Δ (Å)	5.0	10.0, [i] 1.8, [j] 4.8, [k] 4.3 [l]

[a]Reference 39.
[b]Reference 40.
[c]Reference 41.
[d]Reference 42.
[e]Reference 6.
[f]Reference 43.
[g]Reference 44.
[h]Reference 45.
[i]Reference 46.
[j]Reference 37.
[k]Reference 36.
[l]Reference 1.

of the 2D holes but ignores the oxide image charge effects.[1] Again, intra- and intersubband scattering is taken into account.

C. Monte Carlo procedure

The carrier transport has been computed in terms of a momentum space Monte Carlo procedure for a spatially homogeneous channel with constant electric fields and using the scattering rates discussed above. The equations of motion are integrated with the numerically determined, fully nonparabolic subband dispersions $E_\mu(\mathbf{k})$ in analogy to full band Monte Carlo methods that have been developed previously for bulk.[48] Both the hole dispersion relations $E_\mu(\mathbf{k})$ and the inverse relation $\mathbf{k}(E,\mu)$ have been determined by a 2D discretization of $\mathbf{k}$ space.

The Monte Carlo method requires both the individual as well as the total scattering rates. The latter can only be obtained, for each initial state in subband μ with energy $E_\mu(\mathbf{k})$, by a numerical integration of Eq. (6) over all final states. This amounts to integrating over the wave vectors $\mathbf{q}, q_z$ with the numerically determined 2D band structure.

V. NUMERICAL DETAILS

The one-dimensional (1D) $\mathbf{k}\cdot\mathbf{p}$ Schrödinger equation was solved using finite differencing on an inhomogeneous grid[49] and a standard eigenvalue solver. For the 15 nm Si layer and a 500 nm substrate, a few 100 grid points suffice for obtaining well converged eigenfunctions and eigenvalues. The linear 1D Poisson equation was solved exactly in each iteration and self-consistency has been obtained by relaxation using Broyden's convergence acceleration.[50]

For the carrier trajectories, one needs to determine the carrier energy and velocity for given $\mathbf{k}$ and the wave vector for given energy. These values have been determined by discretizing the 2D Brillouin zone and by linear interpolation between the mesh points. The full 2D Brillouin zone was divided into 320×320 equally spaced mesh points. The integrated scattering rates have been calculated by numerical integration over the two-dimensional Brillouin zone with the linear tetrahedron method for 40 subbands and also using 320×320 wave vectors.[51]

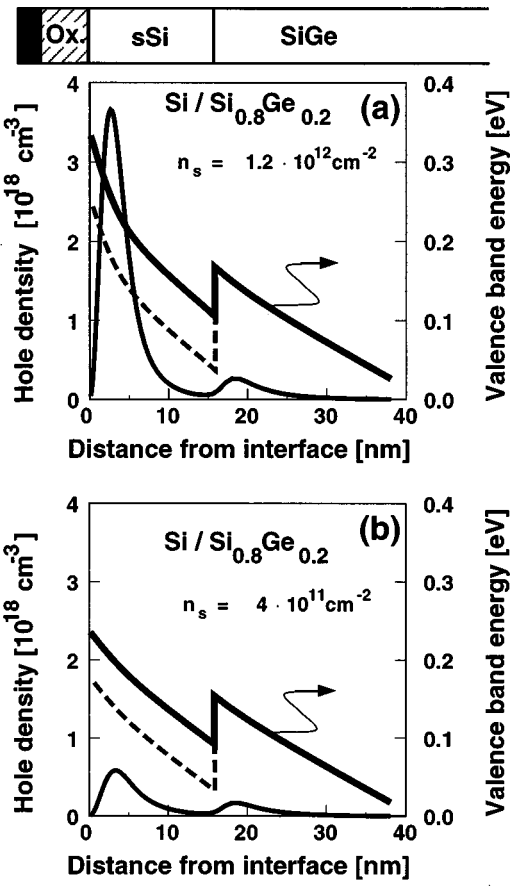

FIG. 2. Calculated valence-band energy (in eV) and hole density (10^{18} cm^{-3}) versus position for a p-type strained Si inversion channel on top of a $Si_{0.8}Ge_{0.2}$ buffer. This cross section is shown along the structure appearing in the top inset and indicated by a dashed line in Fig. 1. The thick full (dashed) lines are the light- (heavy-) hole band-edge energies of bulk strained Si including the Hartree potential. n_s is the inversion layer density and amounts to (a) $n_s=1.2\times10^{12}$ cm^{-2} and (b) $n_s=4\times10^{11}$ cm^{-2}. The doping in the Si and SiGe layers is $N_D=5\times10^{16}$ cm^{-3} in both cases.

VI. RESULTS

A. Self-consistent subbands

When bulk Si gets biaxially strained by a pseudomorphic (001) $Si_{0.8}Ge_{0.2}$ substrate, the light- and heavy hole band split by an amount of 80 meV.[15] Importantly, the top valence-band edge is formed by the light-hole band while the heavy hole band has lower energy. In a MOSFET, the band edge varies spatially due to the confining Hartree potential that forms the inversion channel. In Fig. 2, the light- and heavy-hole valence-band edge energies, including the self-consistently computed Hartree potential, are plotted for a strained $Si/Si_{0.8}Ge_{0.2}$ p-MOS as a function of distance from the oxide interface. Also shown in this figure is the spatially

resolved hole carrier density perpendicular to the channel that results from the occupancy of the bound states in the inversion channel. At room temperature, only the 3–4 highest hole subbands are significantly occupied. In accordance with the band-edge states, the topmost subband has predominantly light-hole character whereas the second, heavy-hole related subband lies 55 meV below.

The results shown in Fig. 2 have been obtained for homogeneously n-doped Si and SiGe with $N_D=5\times10^{16}$ cm^{-3}. By increasing the gate voltage from 1.1 V to 1.6 V (assuming a 5 nm gate oxide), we find the sheet inversion hole charge density $n_s=\int_{-\infty}^{+\infty}p(z)dz$ to increase from $n_s=4\times10^{11}$ cm^{-2} to $n_s=1.2\times10^{12}$ cm^{-2}. Figure 2 clearly shows the formation of the inversion channel. In addition, however, the hole density is seen to possess another, albeit smaller, maximum at the strained-Si/SiGe interface. This parasitic channel is caused by the band discontinuity at this interface and contains almost 30% of the holes for the gate voltage in Fig. 2(b). The influence of this parasitic channel becomes negligible for high gate voltages, such as Fig. 2(a).

B. Drift velocity and energy

In Fig. 3, the low field (average) drift velocity and average kinetic energy is shown as obtained by the Monte Carlo calculations of the 2D hole transport at room temperature. For comparison, we also present results for an unstrained Si channel (on Si substrate). The present results indicate clearly the significantly improved transport characteristics of strained Si on SiGe substrate. In principle, there are two counteracting effects that influence the drift velocity and energy in the inversion channel, namely, the strain induced splitting of the top valence bands and the electric field induced confinement. The strain causes the light-hole band to form the valence band edge so that the holes occupy mainly the light-hole band that leads to a decrease in the conductivity mass and a corresponding increase in velocity. In addition, the band splitting reduces the (predominantly acoustic) intersubband phonon scattering that further enhances the velocity. The confinement of the carriers in the inversion channel, on the other hand, tends to favor the occupancy of the heavy holes since the light holes get pushed to higher energies. However, the latter effect is much smaller than the former, even for small Ge concentrations, i.e., small strain. Finally, there is another confinement effect that originates in the Si/SiGe valence band offset. Since the valence band is energetically lower in Si than in SiGe, this offset tends to delocalize the holes. However, the inversion channel has a width of less than 10 nm (see Fig. 2), which makes this adverse effect negligible as well.

It is instructive to compare the self-consistent results based on the nonparabolic subband structure with a simple model that uses subbands calculated from a single, spherical, effective bulk band with a constant effective mass. Such a model allows one to evaluate the scattering rates analytically. For low fields, we find that the rigorously predicted transport characteristics can be well represented by a single effective parabolic band, as shown in Fig. 3. We note that the effective masses shown in this figure are only slightly higher than the bulk density of states masses that have been calculated previously[6] for holes in strained and unstrained bulk material.

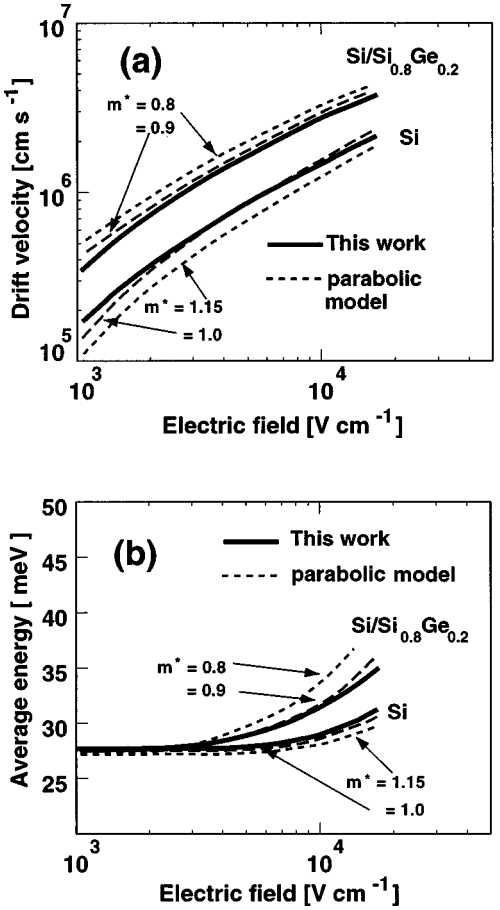

FIG. 3. Solid lines show the calculated (a) drift velocity in cm s^{-1} and (b) average kinetic energy in meV for an unstrained Si p-MOS and for the strained Si/Si$_{0.8}$Ge$_{0.2}$ p-MOS structure. The inversion hole density is $n_s=1.2\times10^{12}$ cm^{-2}. Also shown is a fit of the calculated result to a parabolic one-band model with two different effective hole masses m^* (dashed lines) .

C. Hole mobility in unstrained Si

In Fig. 4, we show the low field hole mobility for unstrained Si p-inversion layers as a function of the sheet hole density n_s, as computed with the self-consistent multiband model of Sec. IV. We have decomposed the calculated hole mobility into separate contributions due to phonon (μ_{ph}), ionized impurity (μ_{imp}), and surface roughness (μ_{SR}) scattering. These partial mobilities are plotted in Fig. 4 and have been obtained by calculating the difference between the total mobility and the mobility that results from artificially switching off that particular scattering mechanism.

These partial mobilities exhibit clear trends as a function of sheet density. The contribution due to phonons scales with $\mu_{ph}\sim n_s^{-1/3}$ in accordance with the corresponding $n_s^{-1/3}$ dependence of the envelope form factor $J_{\mu\nu}$.[9,52] The surface roughness scattering rate[3] yields $\mu_{SR}\sim(n_s+N_{charge})^{-2}$ which suppresses the mobility at high densities. Impurity scattering is only effective for small carrier concentration and becomes unimportant for higher n_s due to screening. Based on the analytic form of the impurity scattering rate, one expects an approximately linear dependence on the density in the low field regime, which is indeed what we find.[3] Altogether, we find the hole mobility to be dominated by

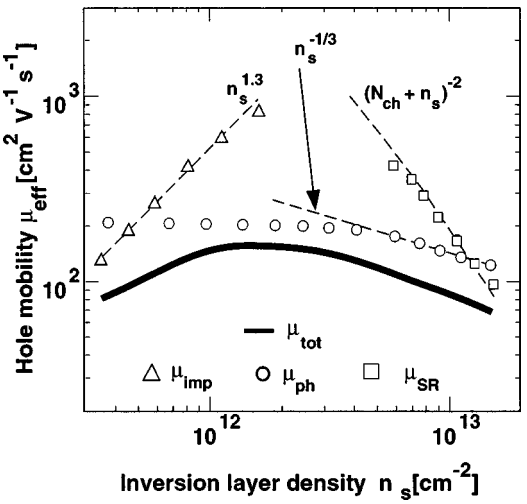

FIG. 4. Thick line shows calculated hole mobility (in $cm^2\ V^{-1}\ s^{-1}$) as a function of the inversion hole density (in cm^{-2}) in unstrained Si p-MOSFET at room temperature. The symbols indicate the separate contributions due to phonon, ionized impurity, and surface roughness scattering, respectively. The dashed lines only guide the eye.

phonon scattering for intermediate densities and by surface roughness scattering in the limit of high n_s.

Experimental low field hole mobilities in MOS devices are often given as a function of the effective normal field that is defined by[53]

$$E_{eff}=\frac{e}{\epsilon}\left(\frac{1}{3}n_s+N_{charge}\right),$$

$$N_{charge}=\int (N_D(z)-n(z))dz, \tag{8}$$

where N_{charge} is the sheet density of the ionized impurities, integrated along the dashed line in Fig. 1. This definition

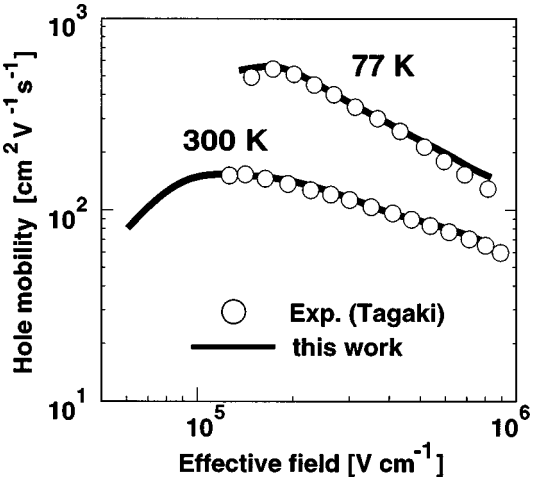

FIG. 5. Calculated hole mobility (in $cm^2\ V^{-1}\ s^{-1}$) of unstrained Si p-MOSFET at two different temperatures as a function of the effective electric field (in V cm^{-1}) as defined in the main text. The symbols indicate experimental results (Ref. 53).

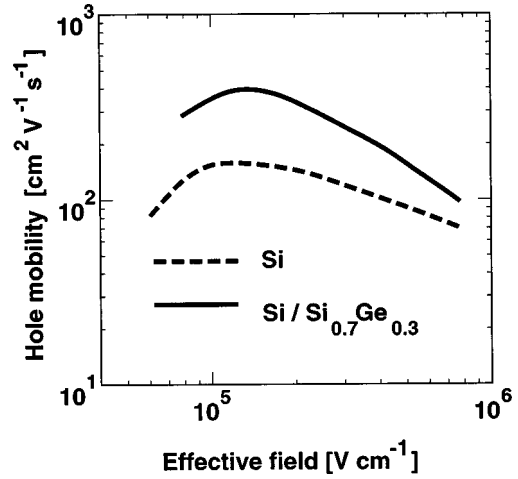

FIG. 6. Calculated room-temperature hole mobility (in $cm^2\ V^{-1}\ s^{-1}$) in strained $Si/Si_{0.7}Ge_{0.3}$ p-MOSFET (solid line) and in unstrained Si p-MOSFET (dashed line) as a function of the effective electric field.

allows one to represent mobilities in a way that is approximately independent of the substrate doping.

In Fig. 5, we compare the present theoretical predictions for the hole mobility as a function of E_{eff} and for two different temperatures with the experimental data,[53] using the physical parameters given in Table III. As can be seen, we find excellent agreement with experiment. This shows that subband quantization plays a determining role for p-inversion layers. The good agreement for both 77 and 300 K is particularly noteworthy and confirms the accuracy of the present model for inter- and intrasubband phonon scattering.

D. Hole mobility in strained Si/SiGe

We now turn to the hole mobility in strained Si/SiGe p-MOSFET's. We have studied relaxed buffers with up to 50% Ge concentrations. In the calculations, we have assumed that the quality of the Si/oxide interface does not

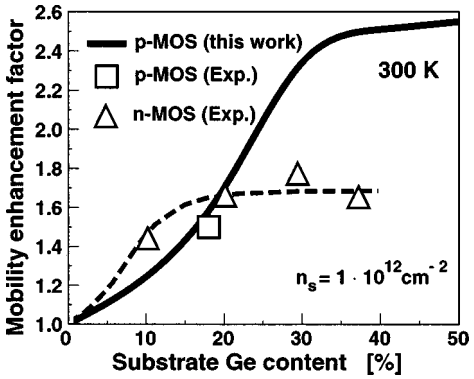

FIG. 7. Calculated ratio of mobility in strained Si/SiGe p-MOS structure to an unstrained pure Si p-MOS structure (solid line). The horizontal axis gives the Ge content of the SiGe buffer that provides the strain in the Si layer. The experimental result (Ref. 10) is indicated by a square. For comparison, we also include experimental results (Ref. 4) in strained Si/SiGe n-type MOS transistors (triangles). The dashed line only guides the eye.

deteriorate with increasing Ge concentration of the buffer and used the same interface roughness parameters throughout.

In Fig. 6, we show the predicted hole mobility for a 30% Ge concentration, as obtained with the present Monte Carlo calculations. For comparison, the figure also shows the result for unstrained Si that had been discussed in the previous section. We predict the hole mobility in strained Si/SiGe to be significantly higher than in pure Si inversion layers, which is consistent with the higher drift velocity that we found in Sec. VI B. By systematically varying the Ge concentration, we find the maximum mobility enhancement to be a factor of 2.5 and to saturate for Ge compositions larger than 40%, as shown in Fig. 7. For $Si/Si_{0.7}Ge_{0.3}$, the maximum hole mobility exceeds that one of pure Si already by a factor of 2.3. The saturation is caused by an almost complete transfer of the holes into the light hole band for sufficiently large strain. A similar effect is known experimentally for the electron mobility in strained Si/SiGe *n*-MOS structures that is also depicted in Fig. 7 for comparison. The present predictions appear to be in excellent agreement with the only published experimental result[10,54] of the hole mobility in strained Si MOS channels (with 18% Ge concentration; see Fig. 7) that we are aware of.

VII. CONCLUSIONS

In conclusion, we have presented a detailed study of the low field mobility in strained *p*-Si/SiGe MOSFET structures that fully takes into account the quantum confined carrier dynamics. We predict a mobility enhancement factor up to 2.3 for Ge concentrations of 30% in the substrate and even higher enhancements for higher Ge content. Our calculations are in excellent agreement with experiment, both for strained Si/SiGe as well as for unstrained Si *p*-MOSFET's.

[1] T. Ando, A. B. Fowler, and F. Stern, Rev. Mod. Phys. **54**, 437 (1982).
[2] M. Shirahata, K. Taniguchi, and C. Hamaguchi, Jpn. J. Appl. Phys., Part 1 **26**, 1447 (1987).
[3] M. V. Fischetti and S. E. Laux, Phys. Rev. B **48**, 2244 (1993).
[4] S. Takagi, J. L. Hoyt, J. J. Welser, and J. F. Gibbons, J. Appl. Phys. **80**, 1567 (1996).
[5] J. M. Hinckley, V. Sankaran, and J. Singh, Appl. Phys. Lett. **55**, 2008 (1989).
[6] M. V. Fischetti and S. E. Laux, J. Appl. Phys. **80**, 2234 (1996).
[7] F. M. Bufler, P. Graf, S. Keith, and B. Meinerzhagen, Appl. Phys. Lett. **70**, 2144 (1997).
[8] D. K. Nayak and S. K. Chun, Appl. Phys. Lett. **64**, 2514 (1994).
[9] S. Kawaji, J. Phys. Soc. Jpn. **27**, 906 (1969).
[10] Deepak K. Nayak, K. Goto, A. Yutani, J. Murota, and Y. Shiraki, IEEE Trans. Electron Devices **43**, 1709 (1996).
[11] K. Brunner (unpublished).
[12] G. Dresselhaus, A. F. Kip, and C. Kittel, Phys. Rev. **98**, 368 (1955).
[13] J. M. Luttinger, Phys. Rev. **102**, 1030 (1956).
[14] G. L. Bir and G. E. Pikus, *Symmetry and Strain-Induced Effects in Semiconductors* (John Wiley, New York, 1974).
[15] M. M. Rieger and P. Vogl, Phys. Rev. B **48**, 14 276 (1993).
[16] C. Y. P. Chao and S. L. Chuang, Phys. Rev. B **46**, 4110 (1992).
[17] Y. X. Liu, D. Z. Y. Ting, and T. C. McGill, Phys. Rev. B **54**, 5675 (1996).
[18] Q. G. Zhu and H. Kroemer, Phys. Rev. B **27**, 3519 (1983).
[19] C. Aversa and J. E. Sipe, Phys. Rev. B **49**, 14 452 (1994).
[20] R. Balian, D. Bessis, and G. A. Mezincescu, Phys. Rev. B **51**, 17 624 (1995).
[21] G. P. Schwartz, M. S. Hybertsen, J. Bevk, R. G. Nuzzo, J. P. Mannaerts, and G. J. Gualtieri, Phys. Rev. B **39**, 1235 (1989).
[22] A. D. Katnani and G. Margaritondo, Phys. Rev. B **28**, 1944 (1983).
[23] E. T. Yu, E. T. Croke, T. C. McGill, and R. H. Miles, Appl. Phys. Lett. **56**, 569 (1990).
[24] L. Colombo, R. Resta, and S. Baroni, Phys. Rev. B **44**, 5572 (1991).
[25] J. D. Wiley, Solid State Commun. **8**, 1865 (1970).
[26] L. D. Laude, F. H. Pollak, and M. Cardona, Phys. Rev. B **3**, 2623 (1971).
[27] M. Costato and L. Reggiani, Phys. Status Solidi B **58**, 471 (1973).
[28] C. Tserbak, H. M. Polatoglou, and G. Theodorou, Phys. Rev. B **47**, 7104 (1993).
[29] C. G. Van de Walle and R. M. Martin, Phys. Rev. B **34**, 5621 (1986).
[30] M. Cardona and F. H. Pollak, Phys. Rev. **142**, 530 (1966).
[31] P. Friede, M. S. Hybertsen, and M. Schleuter, Phys. Rev. B **39**, 7974 (1989).
[32] O. Madelung, in *Tables Numerical Data and Functional Relationships in Science and Technology*, edited by O. Madelung, M. Schulz, and H. Weiss, Landolt-Börnstein, New Series, Group III, Vol. 17, Pt. a (Springer, Heidelberg, 1982).
[33] R. A. Logan, J. M. Rowell, and F. A. Trumbore, Phys. Rev. **136**, A1751 (1964).
[34] L. W. Wang and Z. Zunger, Phys. Rev. B **54**, 11 417 (1996).
[35] F. Szmulowicz, Phys. Rev. B **34**, 4031 (1983).
[36] S. M. Goodnick, D. K. Ferry, C. W. Wilmsen, Z. Liliental, D. Fathy, and O. L. Krivanek, Phys. Rev. B **32**, 8171 (1985).
[37] S. Yamakawa, H. Ueno, K. Taniguchi, C. Hamaguchi, K. Miyatsuji, K. Masaki, and U. Ravaioli, J. Appl. Phys. **79**, 911 (1996).
[38] R. M. Feenstra and M. A. Lutz, J. Appl. Phys. **78**, 6091 (1995).
[39] K. Takeda, A. Taguchi, and M. Sakata, J. Phys. C **16**, 2237 (1983).
[40] M. Fischetti, IEEE Trans. Electron Devices **38**, 634 (1991).
[41] C. Jacoboni and L. Reggiani, Rev. Mod. Phys. **55**, 645 (1983).
[42] Jim Dewey and M. A. Osman, J. Appl. Phys. **74**, 3219 (1993).
[43] J. M. Hinckley, J. Singh, J. Appl. Phys. **76**, 4192 (1994).
[44] T. Yamada and D. K. Ferry, Solid-State Electron. **38**, 881 (1995).
[45] G. Ottaviani, L. Reggiani, C. Canali, F. Nava, and A. Alberigi-Quaranta, Phys. Rev. B **12**, 3318 (1975).
[46] T. Yamada, H. Miyata, J. R. Zhou, and D. K. Ferry, Phys. Rev. B **49**, 1875 (1994).
[47] P. J. Price, Ann. Phys. (N.Y.) **133**, 217 (1981).
[48] M. V. Fischetti and S. E. Laux, Phys. Rev. B **38**, 9721 (1988).
[49] I. H. Tan, G. L. Snider, L. D. Chang, and E. L. Hu, J. Appl. Phys. **68**, 4071 (1994).

[50] D. Singh, H. Krakauer, and C. S. Wang, Phys. Rev. B **34**, 8391 (1986).
[51] G. Wiesenekker, G. te Velde, and E. J. Baerends, J. Phys. C **21**, 4263 (1988).
[52] C. Hamaguchi, Physica (Utrecht) **134**, 87 (1985).
[53] S. Takagi, A. Torimuri, and H. Tango, IEEE Trans. Electron Devices **41**, 2367 (1994).
[54] C. K. Maiti, L. K. Bera, S. S. Dey, D. K. Nayak, and N. B. Chakrabarti, Solid-State Electron. **41**, 1836 (1997).